Laser processing of Crofer22APU and 3YSZ: an interlocking approach for improved interfaces with glass-based seals in solid oxide electrolysers

Ceramics International 51 (2025) 46191–46201

Contents lists available at ScienceDirect

Ceramics International

journal homepage: www.elsevier.com/locate/ceramint

Laser processing of Crofer22APU and 3YSZ: an interlocking approach for improved interfaces with glass-based seals in solid oxide electrolysers

F. D'Isanto [a,*,1], S. Anelli [a,1], F. Puleo [b], M. Salvo [a], D.M.N. Menon [a], S. Márquez [c], D. Janner [a], E. Zanchi [a], A.G. Sabato [c], A. Tarancón [c,d], F. Smeacetto [a]

[a] Department of Applied Science and Technology (DISAT), Politecnico di Torino, Corso Duca Degli Abruzzi 24, 10129, Torino, Italy
[b] Department of Energy (DENERG), Politecnico di Torino, Corso Duca Degli Abruzzi 24, 10129, Torino, Italy
[c] Nanoionics and Fuel Cells, Catalonia Institute for Energy Research (IREC), Sant Adrià de Besòs, 08930, Barcelona, Spain
[d] ICREA, Passeig Lluís Companys 23, 08010, Barcelona, Spain

ARTICLE INFO

Handling Editor: Dr P. Vincenzini

Keywords:
Glass-ceramic sealants
SOEC
Laser processing
Surface tailoring
3D printing
Hydrogen

ABSTRACT

Since glass-to-metal joining reliability over a pressure difference is key in preventing gas mixing and consequent stack failure, enhanced surface-modified interconnect-sealant interfaces represent a specific focus in solid oxide electrolysers integration. This study successfully applied laser surface patterning to Crofer22APU and 3 mol% yttria-stabilized zirconia (3YSZ) substrates, enabling reproducible and controlled texturing. Mechanical testing confirmed that such patterning considerably improved joint strength, with no measurable adhesion in untreated samples and peak mechanical resistance reaching approximately 34 MPa in laser-treated Crofer/Crofer and Crofer/3YSZ configurations. A new composite glass-based paste was developed using a 3YSZ-based approach, showing the proper balance of an adequate design of the interconnect roughness while avoiding significant defects at the glass-to-metal interface. This formulation incorporated 10 wt% 3YSZ into the glass matrix, significantly increasing the high-temperature viscosity (from $10^{4.8}$ to $10^{6.1}$ Poise) and enhancing processing stability and application performance. The composite paste exhibited excellent rheological properties, with viscosities in the 10–100 Pa s range and 80 % recovery after high shear stress (200 s^{-1}), making it highly suitable for robocasting. Importantly, the robocasted glass structures with laser-patterned surfaces withstood pressure differentials of up to 4 bar, demonstrating robust sealing performance. Leak-tightness was further validated through nitrogen pressure difference tests up to 4 bars without any detectable leakage.

1. Introduction

Hydrogen is considered a strategic enabler promoting the energy transition. It is driving a new industrial revolution with positive returns regarding economic growth, employment, and energy security. The production of green hydrogen via electrolysis using electricity to split water or, more generally, Power-to-X (P2X) technology, plays a key role in the decarbonisation of energy-intensive sectors (e.g., iron and steel, refineries, ceramics industry or chemical plants), and in particular for the massive energy storage of electricity continuously generated by renewable energy sources (mainly wind and solar) [1]. According to European Hydrogen strategic guidelines, 40 GW of electrolysis plants will be installed by 2030 in Europe [2]. Solid oxide electrolysis cell (SOEC) technology, which operates at elevated temperatures ranging from 600 °C to 900 °C, has gained special attention for generating pure hydrogen, thanks to its higher efficiency than low-temperature electrolysis technologies [3–6]. Furthermore, SOEC presents high production yields and low specific electric energy consumption (<40 kWh/kg of H_2) [7], in comparison with competing technologies such as alkaline electrolysers (around 55 kWh/kg of H_2) and proton exchange membrane electrolysis cells (around 53 kWh/kg of H_2) [8,9].

One of the significant challenges in designing long-term reliable solid oxide cell stacks is the selection of joining materials for sealing the metallic interconnect and the ceramic electrolyte [10]. The most common sealants are glass-ceramics due to the sinter-crystallization process's simplicity and the possibility of tailoring their composition and thermo-mechanical properties, providing electrical insulation and preventing gas mixing [11–15]. In particular, the sealing in electrolysis

* Corresponding author.
E-mail address: fabiana.disanto@polito.it (F. D'Isanto).
[1] Equal contribution to the paper.

https://doi.org/10.1016/j.ceramint.2025.07.326
Received 29 April 2025; Received in revised form 15 July 2025; Accepted 23 July 2025
Available online 23 July 2025

equipment presents significant challenges in ensuring efficiency, maintaining the separation of hydrogen and oxygen gases. In this sense, one of the main issues is to improve the adhesion at the interface between the glass sealant and the materials of the SOEC stack. Previous investigations proved that a surface pre-treatment is an effective procedure to improve the adhesion, leading to a cohesive fracture of the sealant during mechanical testing. In general, to exploit the joining material's mechanical strength, several surface treatments are typically performed before joining similar or dissimilar materials (i.e., metal-to metal [16,17], polymer-to metal [18], ceramic-to-ceramic [19], metal-to-glass [20], etc.). In particular, in the area of SOC applications, Ritucci et al. [20] examined the interface adherence of joints made of Crofer22APU interconnects after three different surface treatments and containing a diopside-based glass-ceramic as joining material. The adhesion was assessed by measuring the fracture energy, although the effect of the surface roughness on the glass-to-metal adhesion was not discussed. Other authors showed that a suitable metal roughness is required to maximize the mechanical interlocking effect in a glass-to-metal joint. F. Smeacetto et al. [21] reported that the torsional shear strength of glass-joined Crofer22APU increased 30 % when a laser pre-treatment was applied. This improvement was attributed to the mechanical interlocking effect resulting from the glass infiltration into the laser-induced protrusions on the metal surface.

Another issue affecting the mechanical strength of the glass-ceramic sealing is the reproducibility and the scalability of its deposition. Robocasting was chosen as the deposition technique to ensure a controlled thickness and uniform deposition of the sealant along the surface [22,23]. Robocasting or direct ink writing is an extrusion-free forming Additive Manufacturing technique where viscous slurry filaments are extruded through a nozzle [24]. Robocasting is a scalable and reproducible deposition technique with a minimum waste of ink compared to other slurry-based methods, and it is currently used to build catalyst supports [25], biocompatible scaffolds [26], materials for environmental applications [27], electrochemical materials for energy storage, etc. [24,28]. Moreover, robocasting or other extrusion-free forming techniques can be effectively used for a reliable deposition of glass sealing for SOEC applications [22,23,29,30]. Aiming to obtain a reproducible, continuous and gas-tight glass sealant with good shape retention, optimized rheological properties are required [22].

This work is focused on the design of sealing solutions using 3D-printed SOEC cells and optimized glass-based sealants with enhanced adhesion achieved through surface modification on Crofer22APU and 3YSZ components, able to withstand a significant differential pressure, i.e., up to 4 bars. The refractoriness of a commercial glass-ceramic sealant using a composite approach was successfully improved, significantly enhancing the performance under operational conditions. Additionally, a laser patterning process applied to Crofer22APU and 3YSZ components was optimized, enabling precise surface modifications that enhanced mechanical interlocking and adhesion. These advancements improved the mechanical resistance of the joined samples, which was further validated through pressure difference testing. The results demonstrated the robustness of the glass-ceramic sealant, proving its capability to withstand high-pressure differentials.

2. Experimental

2.1. Glass-ceramic sealants selection, thermal and rheological characterisation

In this study, similar (Crofer/Crofer) and dissimilar (Crofer/3YSZ) joined samples were produced using Crofer22APU steel interconnects (VDM Metals, Verdohl, Germany) and 3-yttria-stabilized zirconia (3YSZ) 3D-printed electrolytes (3DCERAM, Limoges, France). The joining material was a glass-ceramic sealant produced from a glass-based paste formulated for robocasting deposition, starting from a commercial glass (G018-392, $d_{50} = 10 \pm 2$ μm and $d_{99} \leq 63$ μm), specifically developed by SCHOTT AG (Landshut, Germany) for the hermetic sealing and joining of interconnects to prevent the uncontrolled exchange of gas, enabling excellent long-term gas tightness at high temperatures and after thermal cycling [31]. The glass composition provided by the company is shown in Table 1.

Furthermore, 3YSZ (3DCERAM, Limoges, France) microfine powder with $d_{50} = 0.7$ μm was added to the sealing glass to create a composite, to improve the viscosity as well as to obtain a better thermo-mechanical and chemical compatibility with the electrolyte material (3YSZ). The as-received commercial glass (labelled as "Glass") and a mix of glass matrix and 5 wt% and 10 wt% of 3YSZ powder, labelled as "Glass + 5 wt% 3YSZ" and "Glass + 10 wt% 3YSZ", respectively, were thermally characterised through differential scanning calorimetry (DSC) and hot stage microscopy (HSM), which were carried out to study the influence of 3YSZ addition on the characteristic temperatures of the glass system and to define boundary conditions to optimize the sealing procedure. DSC analyses (DSC 404 F1/F3 Pegasus, Netzsch, Selb, Germany) were conducted to investigate the crystallization behaviour from room temperature to 950 °C. From each thermogram, glass transition temperature (T_g), crystallization onset temperature (T_x) and crystallization peak temperature (T_p) were extrapolated. The T_g was evaluated as the onset of the endothermic transformation related to the glass transition in the DSC curves. T_x and T_p are, respectively, the crystallization's onset and peak. HSM measurements (EM, 301 Hesse Instruments, Harzgerode, Germany) were performed to evaluate the sintering of the systems under study. The sample for HSM was a cylindrical pellet (3 mm diameter and 3 mm height) obtained by uniaxially pressing the powders with some drops of ethanol. The measurements were conducted by placing the sample on an alumina support, from room temperature up to the melting point identified by the instrument. The HSM built the sample image through a quartz window onto the recording device. The computerised image analysis system automatically recorded and analysed the sample geometry. Based on the shape and dimension assumed by the samples during the heat treatment, the instrument automatically determined six specific points in the deformation and flow rates according to geometrical considerations: first shrinkage temperature (T_{fs}), maximum shrinkage temperature (T_{ms}), deformation temperature (T_D), sphere temperature (T_S), half-sphere temperature (T_H), and flow temperature (T_F). All these treatments were conducted at a 5 °C/min heating rate under flowing air. Using the six experimental viscosity points previously identified for each system under study, fitting to the Vogel-Fulcher-Tamman (VFT) equation for viscosity below 10^{10} Poise was performed [32]. The constants of the equation were calculated by linear regression, fitting all the experimental data with $\log \eta < 10$ to the function $\eta(T) = A + B/(T\text{-}T_0)$, and changing the value of the constants A, B, and T_0 until the highest level of the regression coefficient (R^2).

Considering the results obtained through thermal analysis assessments concerning the influence of 3YZ addition on the characteristic temperatures of the glass systems, some pastes were produced by a mixture of glass and additives with a solid load of 75 wt% and 80 wt%, labelled as P0-75 and P0-80, respectively, while some pastes were produced by a mix of glass matrix and the addition of 10 wt% of 3YSZ powder, with a solid load of 75 wt% and 80 wt% and were labelled P10-75 and P10-80. Propylen glycol (Sigma Aldrich) was used as a solvent and two types of Polyvinylpolypyrrolidone (PVP) were used as

Table 1
Chemical composition in mol% of G018-392 commercial glass provided by SCHOTT AG.

Composition	mol%
RO (R=Ba, Ca, Zn)	~50
B_2O_3	< 15
Al_2O_3	< 2
SiO_2	balance

dispersant and binder, respectively, PVP K30 (Sigma Aldrich) and PVP K90 (Sigma Aldrich). The dispersant was always kept at 1 wt% of the total solid loading, and the binder was at 1 wt% of the total liquid amount. The glass-based pastes have been prepared by mixing the components in a planetary mixer (ARE-250 CE THINKY, USA). The organic part was first mixed at 1400 rpm min^{-1} for 10 min. The solid loading was added in 6 steps of 5 min each: four at 1400 rpm min^{-1} and the last two at 1600 rpm min^{-1}. All glass-based pastes, listed in Table 2, were rheologically characterised, to select the most suitable one for the deposition and obtain a sealant with the best interfacial compatibility with the substrates.

The rheological properties of the formulated pastes were assessed by an HR-2 rheometer (TA Instruments, USA) with a plate-plate geometry with a diameter of 25 mm. All the rheological characterisations have been performed at 25 °C, and two types of tests were conducted:

i) Flow sweep test, where the dependence on the shear rate of the viscosity is studied. The shear rate is varied during the experiment from 0.01 to 500 s^{-1}.
ii) The five interval thixotropy test is carried out to investigate the elastic recovery of the robocasting paste. Here, two shear rate values, 10 and 200 s^{-1}, are applied at an interval of 60 s, to study the viscoelastic behaviour of the paste after a considerable solicitation.

2.2. Surface modifications, joining, and mechanical tests

To improve the chemical bond between sealants and stack materials, e.g., Crofer22APU and 3YSZ, surface modifications were made with an Infrared Nanosecond fibre laser with the following parameters: wavelength = 1064 nm, pulse width = 12 ns, spot size = 60 μm. After a systematic optimization of the laser processing parameters, conducted by varying one parameter at a time, while monitoring surface quality, processing efficiency, and material integrity, the following values were selected as optimal: scan speed of 15 mm s^{-1}, pulse repetition rate of 20 kHz, lateral scan spacing of 60 μm, and average laser power of 20 W. These conditions provided the best compromise between processing speed and surface quality and ensuring process stability.

After each surface modification and before further processing, Crofer22APU samples were sonicated in acetone and ethanol solutions for 5 min each to remove any eventual residue that might have formed on the surface during laser processing. The surface morphology of the samples was analysed via a stylus profilometer (Form Talysurf Intratouch, Taylor Hobson, USA). A selected surface area of 0.75 mm^2 (1.5 mm × 0.5 mm) was scanned, and the physical parameters of the surface in terms of average surface roughness (S_a) and the maximum peak to valley height (S_z) were derived [21]. Afterward, the FE-SEM observed top views and cross-sectioned samples of lasered Crofer22APU (L-Crofer) and lasered 3YSZ (L-3YSZ) to investigate the surfaces' texture after the laser modification.

Based on the results obtained from the DSC and HSM analyses and the rheological measurements, one composition was selected, and sandwich-like structure samples were prepared following the scheme in Fig. 1a and b. The joining process involved applying the glass-based paste using a syringe onto one Crofer22APU plate (similar joints) or the 3YSZ (dissimilar joints) plate before assembling the components according to the respective configuration, to obtain the following joints: Crofer/L-Crofer, L-Crofer/L-Crofer, Crofer/L-3YSZ, and L-3YSZ/L-3YSZ, where "L-" means "lasered" surfaces. Subsequently, the samples were dried in an oven at 98 °C for 25 min. Finally, they were joined in a muffle furnace (L5/13/P330, Nabertherm GmbH, Lilienthal/Bremen, Germany). Subsequently, the samples were dried in an oven at 98 °C for 25 min. Finally, they were joined with a 15 g/cm^2 weight on top, with the following thermal treatment in static air:

- 2 °C/min up to 120°C- 1 h dwell
- 2 °C/min up to 300°C- 1 h dwell
- 3 °C/min up to 900°C- 1 h dwell
- 1 °C/min down to 300°C-1 h dwell

The apparent shear strength of Crofer/Crofer and Crofer/3YSZ joined samples was evaluated using the single lap offset (SLO) test under compression according to a method adapted from ASTM D905-08 [33]. The samples for mechanical tests were produced following the scheme shown in Fig. 2a and b. In particular, SLO joints were prepared in different configurations to study the positive effect of the surface modification on the mechanical resistance. The different SLO joints were prepared: i) both sides lasered, ii) only one side lasered, and iii) only as received surfaces. For each configuration, three specimens were prepared. After joining, the specimens were gently polished for a few minutes to ensure the steel and ceramic plates were perfectly parallel. The fixtures were placed to minimize the substrates' bending and rotation [34] (Fig. 2c). Mechanical tests were carried out with a universal testing machine (Syntec D/10, MTS Corp.) equipped with a 50 kN load cell and a 0.5 mm/min crosshead speed. The maximum force was recorded, and the apparent shear strength was calculated by dividing the maximum force by the joining area. The size of the single lap offset shear tests for joined samples was about 25 mm × 12.5 mm × 3 mm. All the fracture surfaces were observed and macroscopically characterised; the results of the mechanical tests were expressed as mean ± standard deviation.

2.3. Tests in differential pressure

Differential pressure test was performed on a joined sample consisting of a Crofer22APU plate with a tube welded at the centre and a 3D-printed 3YSZ plate of both 5 × 5 cm^2; the schematic configuration is shown in Fig. 3a. Both of them were lasered, as shown for Crofer22APU in Fig. 3b, and subsequently they were joined using a glass-based paste. The P10-80 paste was deposited by robocasting (ZMorph S.A., Poland) with a conical nozzle with a hole diameter of ≈1.2 mm (Fig. 3c), and the Crofer and YSZ plates were joined at 900 °C for 1 h, with the same thermal treatment applied for smaller joints (Fig. 3d). The sample was tested at 2.1, 3.1 and 4.1 bars with N_2 at room temperature.

2.4. Microstructural characterisation

The morphological and compositional characterisation of top-view and cross-sectioned Crofer22APU and 3YSZ lasered substrates, cross-sectioned of both as-joined and mechanically tested samples, was assessed using a high-resolution field emission electron microscopy (FE-SEM, Zeiss Supra 40, Oberkochen, Germany) equipped with an energy-dispersive X-Ray spectrometer (EDX) system for elemental analysis. Before the FE-SEM investigation, the cross-sectioned samples were embedded in epoxy resin (Struers, Denmark) and polished using SiC abrasive paper (Hermes Schleifmittel GmbH) with different granulometries (grit size 120–4000). Samples were sputtered with Pt before FE-SEM analysis.

Table 2
Composition of the glass-based pastes under study.

Pastes	Solid loading (wt%)	3YSZ in the solid loading (wt%)	PVP K30 (wt % referred to the solid loading)	PVP K90 (wt% referred to the liquid)	Liquid (wt%)
P0-75	75	–	1	1	25
P10–75	75	10	1	1	25
P0-80	80	–	1	1	20
P10–80	80	10	1	1	20

Fig. 1. Schematic representation of as-joined samples in (a) similar and (b) dissimilar joints.

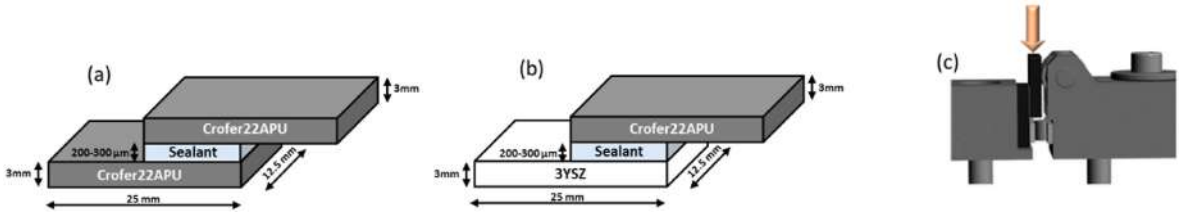

Fig. 2. Schematic representation of as-joined samples for single lap offset (SLO) mechanical test for (a) similar and (b) dissimilar configuration. (c) Configuration of the fixtures to avoid bending and rotation of the substrates during the test.

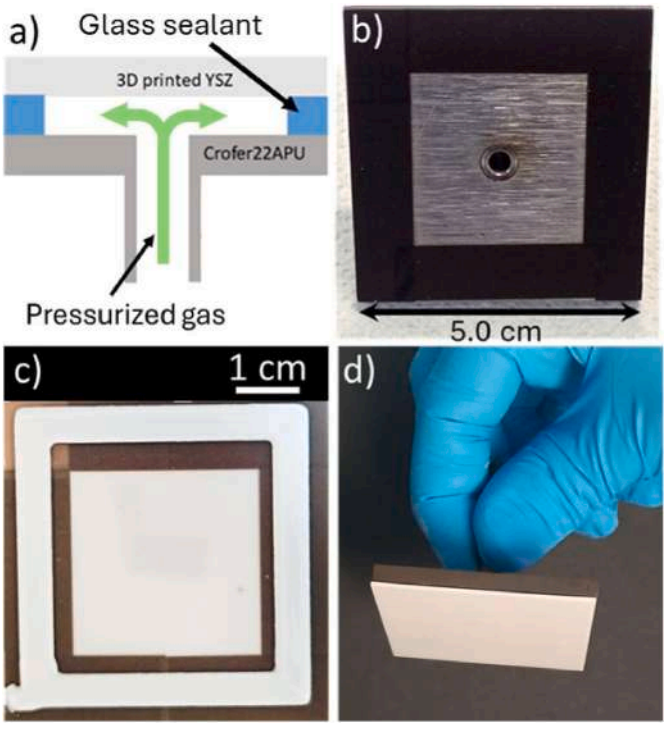

Fig. 3. (a) Schematic view of the differential pressure test. (b) Digital image of the lasered Crofer 22APU plate with the welded tube. (c) Digital image of the deposition by robocasting of the glass-based sealant on the lasered 3YSZ 5 × 5 cm plate. (d) Digital image of the joined 5 × 5 cm Crofer22APU and 5 × 5 cm 3YSZ.

3. Results and discussion

3.1. Characterisation of glass-ceramic sealants

Fig. 4a and b show the experimental data obtained from the DSC and HSM analyses, respectively, performed on a glass sample, a mixture of glass matrix and 5 wt% or 10 wt% of 3YSZ (Glass + 5 wt% 3YSZ and Glass + 10 wt% 3YSZ, respectively). The characteristic temperatures (T_g, T_x, T_p) for all systems under study were extrapolated from the DSC curves shown in Fig. 4a and reported in Table 3. One can observed that T_g values are in the range 578–586 °C, the onset of the crystallization T_x is later than 720 °C and T_p is 745–748 °C, identifying temperatures that are largely consistent for the three systems, within fluctuations of the measurements, concluding that the 3YSZ addition to the pure glass didn't influence the crystallization behaviour. In Fig. 4b, the sintering percentage is plotted against the temperature, and the most evident aspect of this graph is that while the first shrinkage temperature (T_{fs}), which is determined by the glass matrix, wasn't affected by the presence of 3YSZ particles, a different behaviour can be observed after sintering begins. As reported in Table 4, T_{ms} increased from 700 °C in the "Glass" sample to 710 °C and 728 °C in "Glass+5 wt% 3YSZ" and "Glass+10 wt % 3YSZ" samples, respectively. In general, it can be observed that systems composed of glass matrix and yttria-stabilized zirconia particles displayed a delay in terms of characteristic temperatures (T_{ms}, T_D, T_{sp}, T_{hs}, and T_{flow}), more evident with the addition of 10 wt% of 3YSZ, as predicted. Moreover, while the sample with only glass recorded a relative shrinkage of around 35 %, "Glass+5 wt% 3YSZ" and "Glass+10 wt% 3YSZ" samples reached a lower shrinkage of 25 %. Furthermore, a plateau between 700 and 950 °C may be explained by the increase in viscosity due to the devitrification phenomena, which started after 700 °C, as reported from the characteristic temperatures identified through the DSC analysis (T_x in Table 3). Fig. 4c shows a trend line to predict the log viscosity of the systems versus the temperature, obtained by plotting the characteristic temperatures, resulted from HSM curves, at fixed viscosity values shown in Table 4 and reported from M. J. Pascual et al. in [32]. Therefore, considering the characteristic temperatures, it was possible to study, by an indirect method, the viscosity behaviour of the systems at the operating temperature (i.e., 850 °C) as in previous works [15,35,36]. In all curves, experimental viscosity points were fitted calculating the constants of the $y = A + B/(T\text{-}T_0)$ equation and the R-square values (reported in Table 5), by linear regression fitting all the experimental figures with $\log \eta < 10$. It can be highlighted that, at 850 °C, an increase of viscosity from $10^{4.8}$ Poise of the pure glass to $10^{5.4}$ and $10^{6.1}$ Poise of the composites was obtained with the addition of 5 wt% and 10 wt% of 3YSZ powder, respectively. Considering these results, particularly the increase in viscosity due to adding 3YSZ powder, the composite glass-ceramic/3YSZ powder with 90 wt%/10 wt% was the best combination. Therefore, it was used in this work to prepare pastes for robocasting deposition.

3.2. Rheological characterisation of pastes for robocasting

Fig. 5a shows the flow curve measurements, in logarithmic scale, done on two weight percentages (75 % and 80 %) of Schott G018-392 glass powder with and without the addition of 10 wt% of 3YSZ. The

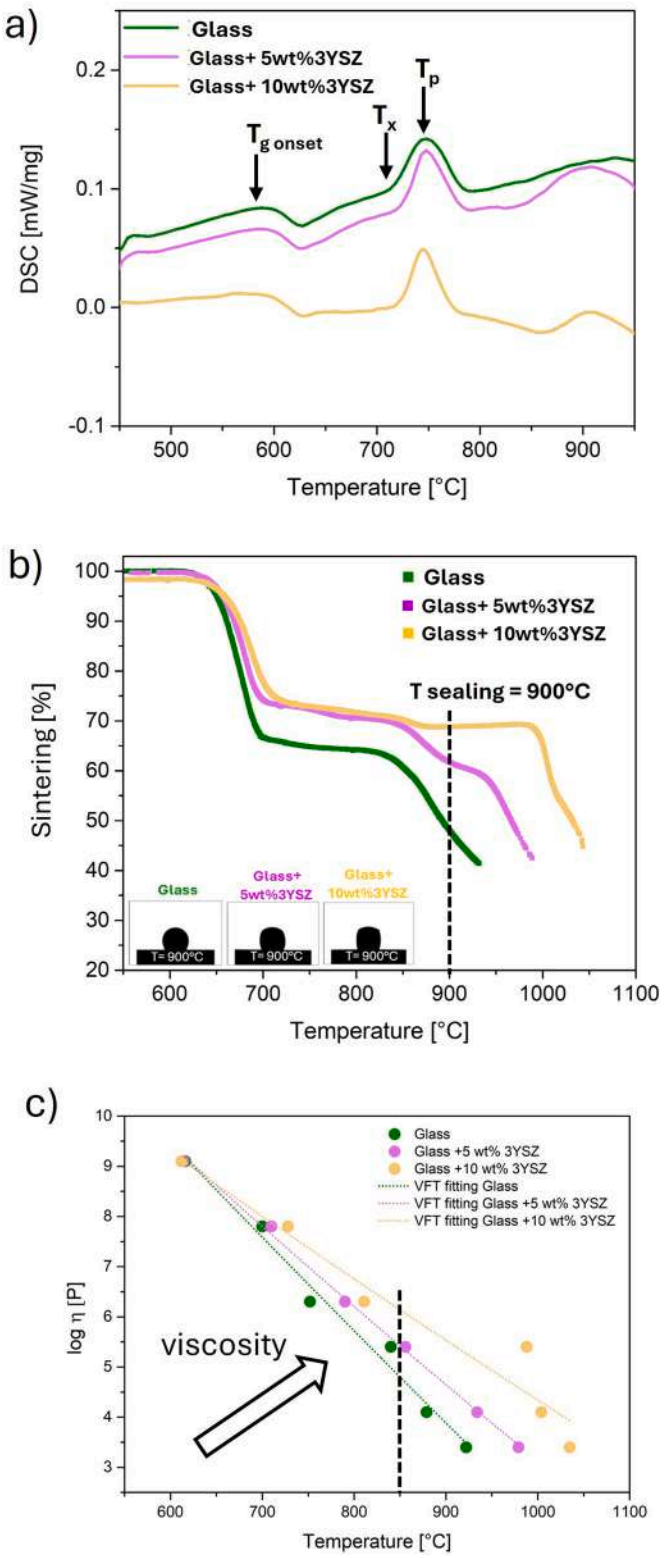

Fig. 4. (a) DSC and (b) HSM analyses of samples produced with 100 wt% glass (Glass), glass with 5 wt%, and glass with 10 wt% of YSZ (Glass+5 wt%3YSZ and Glass+10 wt%3YSZ); profiles of samples' image recorded at 900 °C (sintering temperature) were reported in the inset; (c) log η vs T curves obtained by fitting the characteristic fixed viscosity points and related temperatures [32].

Table 3
Characteristic temperatures of samples produced with 100 wt% glass (Glass), glass with 5 wt%, and glass with 10 wt% of YSZ (Glass+5 wt%3YSZ and Glass+10 wt%3YSZ); all data were obtained by DSC analysis.

Characteristic temperatures	Glass T (°C)	Glass+ 5 wt% 3YSZ T (°C)	Glass+ 10 wt% 3YSZ T (°C)
$T_{g\ onset}$	578	583	586
T_x	718	725	723
T_p	748	748	745

Table 4
Characteristic temperatures at fixed viscosity values for the samples produced with 100 wt% glass (Glass), glass with 5 wt%, and glass with 10 wt% of YSZ (Glass+5 wt%3YSZ and Glass+10 wt%3YSZ). Viscosity values (log η) from [32].

	Glass T (°C)	Glass+ 5 wt% 3YSZ T (°C)	Glass+ 10 wt% 3YSZ T (°C)	log η (Poise)
T_{fs}	616	614	612	9.1
T_{ms}	700	710	728	7.8
T_D	752	790	811	6.3
T_{sp}	840	856	988	5.4
T_{hs}	879	934	1004	4.1
T_{flow}	922	979	1035	3.4

Table 5
Equation parameters and R-square values.

Sample	A (standard error)	B (standard error)	T_0 (standard error)	R-square
Glass	−258.28 (3122.15)	3.77 (8.87)	−13467.36 (166424.34)	0.97
Glass + 5 wt% 3YSZ	−113.19 (222.26)	903868.99 (3.36)	−6770.68 (13950.62)	0.99
Glass + 10 wt % 3YSZ	−97.70 (1144.79)	883670.43 (1.94)	−7660.08 (92549.70)	0.91

addition of 3YSZ powders to the paste composition affected the rheological properties of the pastes, as due to its smaller particle size, the 3YSZ breaks the interaction among the glass particles. Fig. 5a shows that all four pastes present shear thinning behaviour, which is one of the requisites to allow the paste to flow through the nozzle [22,37,38]. Aiming to facilitate the extrusion and retain the deposited shape afterward, an optimal viscosity interval around 10–100 Pa s at high shear rates was reported in the literature [38]. From these considerations, P10-80 is the paste that showed the best rheological behaviour for robocasting deposition. One can observe that P0-80 showed high viscosity, while both P0-75 and P10-75 presented a rheological behaviour that would lead to poor shape retention after deposition.

Fig. 5b shows the five interval thixotropy tests made to study the recovery of the paste upon stress and, therefore, its ability to recover the initial viscosity after the deposition. Considering the viscosity of the first step as a benchmark, the recovery percentage and time of the paste were determined [23,24]. The study of the thixotropic behaviour of a viscous paste is a crucial aspect to consider the shear history of the materials and prevent sagging or levelling effects after deposition [39]. Defects due to poor shape retention can lead to poor reproducibility, inhomogeneities in the deposition, and mechanical stress during the joining thermal treatment, leading to the failure of the joining process.

A good recovery of the original viscosity characterises P0-75 and P10-75, however, the presence of 3YSZ stabilises the rheological properties of the latter, in terms of stability at high share rates and improvement of the viscoelastic behaviour. In fact, after stress at 200 s^{-1} and 60 s at 10 s^{-1}, P0-75 shows a recovery of 74 % (12.3 Pa•s) and 64 % (10.7 Pa•s) of the original viscosity value of 16.6 Pa•s. Adding 3YSZ to P10-75 raised this recovery to 94.5 % (7.2 Pa•s) and 91 % (7.2 Pa•s)

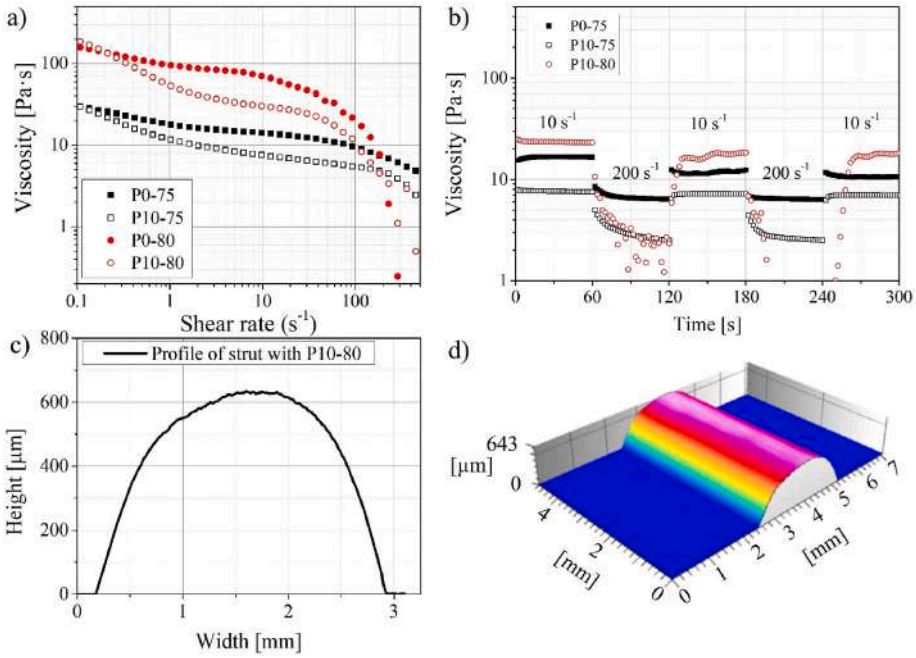

Fig. 5. (a) Flow sweep curves of pastes with solid loading 75 wt% and 80 wt%, with and without 10 %3YSZ. (b) Two interval thixotropy test of pastes with solid loading 75 wt% and 80 wt%, with and without 10 %3YSZ. (c) Profilometer measurements of a printed strut with the paste with 80 wt% of solid loading and 10 % of 3YZ and (d) 3D reconstruction after the measurement.

from the initial value of 7.6 Pa•s. Finally, P10-80 showed a recovery of around 80 % (18.3 Pa•s) after stress at 200 s^{-1} for 60 s at the original share rate value of 10 s^{-1} (23.1 Pa•s).

Considering the shear thinning and thixotropic behaviour, the P10-80 paste was selected for the deposition with robocasting and the preparation of all the samples for mechanical testing.

Finally, Fig. 5c and d show the profilometer measurement and the 3D reconstruction of a printed strut. Before the measurements, the strut was dried for 40 min at 90 °C in an oven. The thickness of the deposited strut is around 640 µm, and the width is around 3 mm.

3.3. Surface modification of Crofer22APU and 3YSZ

The laser processing of the metallic interconnect and the electrolyte was optimized to increase the adhesion at the glass-ceramic/substrate interface. Surface modifications by laser processing to increase the resistance of a joined interface have already demonstrated their effectiveness in a previous work [21]. Laser processing is divided into three different phenomena: target heating, material removal, and plasma shielding [40]. The energy of the laser is absorbed by the target, which overheats. When a critical temperature is reached, the material is removed by phase explosion, i.e., a rapid phase transformation due to laser-induced superheating, which forms both liquid and vapor phases, resulting in material removal. In the case of the present work, the phase explosion is the dominant phenomenon due to the high energy involved in the process [41,42].

Fig. 6a and b show the top view morphology of the L-Crofer and L-3YSZ, respectively, where the pattern of the surface modification can be observed. Fig. 6c and d show the same samples at higher magnification. Small cracks were present on the ceramic surface; their presence is currently under study, and further optimization of the laser processing will be conducted to avoid them. Moreover, it can be observed how the laser processing, made with the same parameters on both surfaces, seemed more effective on Crofer22APU than on 3YSZ. This was confirmed by the profilometer analyses, which showed Sa and Sz parameters of ≈5.0 µm and ≈44.4 µm, respectively, for the Crofer22APU and ≈4.9 µm and ≈32.2 µm for 3YSZ samples.

3.4. Microstructural characterisation of joined samples

Based on the results obtained from thermal and rheological analyses, P10-80 paste has been selected to prepare sandwich-like samples with the scheme of Fig. 1a and b, using the joining procedure described in the experimental section and producing the following specimens: Crofer/L-Crofer, L-Crofer/L-Crofer, Crofer/L-3YSZ and L-Crofer/L-3YSZ. The thermal treatment to consolidate the sealant material was chosen at 900 °C for 1 h, since a value of viscosity around 10^5-10^6 Poise is obtained. This value is suitable for good glass flow and sinterability on the Crofer22APU and 3YSZ substrates. Fig. 7 reports the results of the FE-SEM characterisation of the cross-section of the Crofer/L-Crofer, L-Crofer/L-Crofer, Crofer/L-3YSZ, L-Crofer/L-3YSZ joined samples, observing excellent adhesion of the sealant to both the Crofer and L-Crofer22APU, and L-3YSZ samples, as reported in Fig. 7a–c, e, g. Furthermore, no cracks were detected in the glass-ceramic joining material, demonstrating good thermo-mechanical matching between the glass-ceramic paste and the substrates. Fig. 7b–d, f, h shows that the glass-ceramic infiltrated the crevices of both the L-Crofer22APU and L-3YSZ samples, showing good wettability during the joining thermal treatment. The devitrification of the glass matrix during the sealing process leads to the formation of crystalline phases, which produce a dense network of light, needle-like interlocked crystallites embedded in the residual glassy phase. EDS analysis in Fig. 7f (point 1) revealed mainly the presence of Ba, Si, and O, indicating the crystallization of barium silicate crystalline phase, confirmed by x-ray diffraction analysis (XRD) (reported in Figure S.1 of the supplementary information). $BaSiO_3$ phase was found homogeneously dispersed within the darker glassy matrix, which shows a higher level of Al and Ca and a lower content of Ba and Si (point 2), beneficial to maintain the viscous behaviour of the residual glass. A small Al, Ca, Zn, and Zr concentration was also detected at point 4 in Fig. 7d. However, the morphology of the black phase (point 4) is very similar to the cristobalite phase observed in previous studies [43]. Furthermore, XRD analysis (Figure S.1) confirmed the presence of cristobalite (SiO_2) phase in the glass-ceramic sealant. Even if this crystalline phase is considered potentially dangerous for the integrity of the sealants (due to its volume change around 220 °C [44]), the absence of

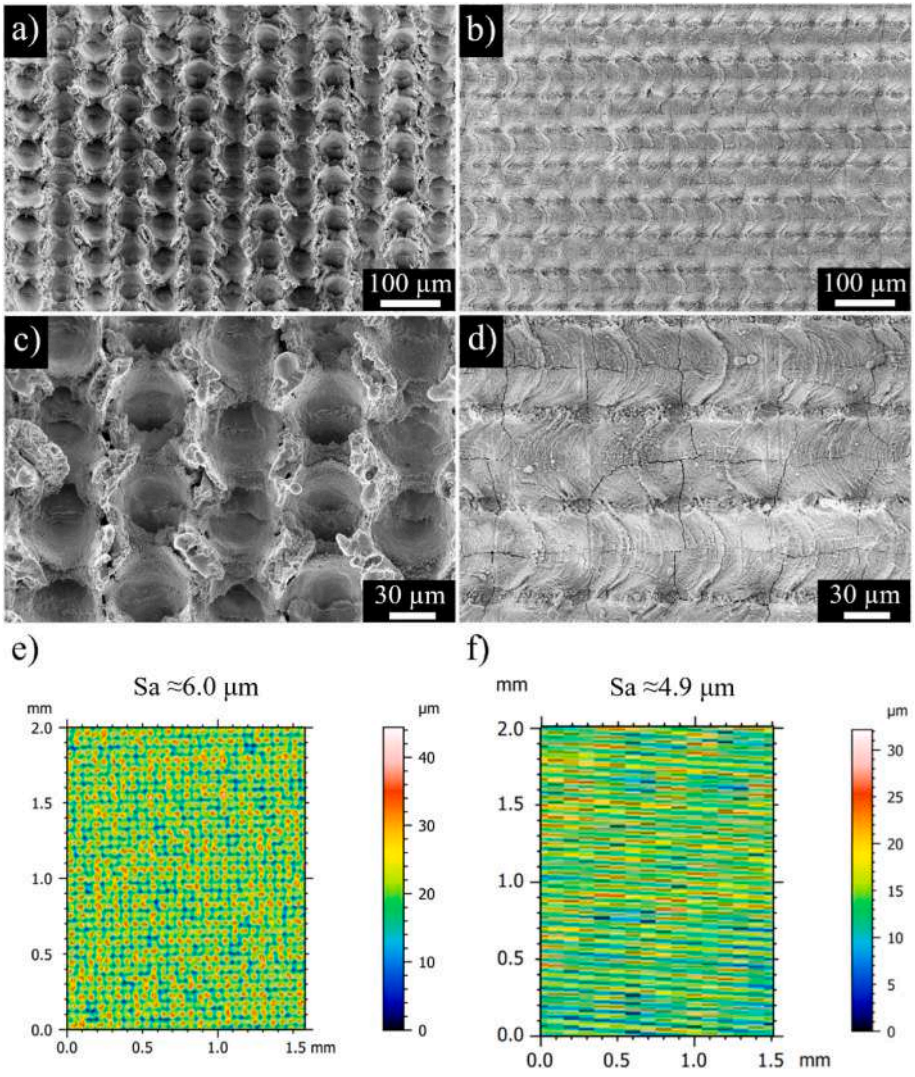

Fig. 6. (a) FE-SEM top-view micrograph of a sample of L-Crofer and (b) a top-view micrograph of L-3YSZ. Higher magnification micrographs of (c) L-Crofer and (d) L-3YSZ, respectively. Profilometer map made on (e) L-Crofer and on (f) L-3YSZ to show the difference in roughness due to the laser processing made on different substrates.

cracks starting from cristobalite particles was visible. Furthermore, the yttrium-stabilized zirconia was homogeneously distributed in the glass-ceramic sealant (point 3).

3.5. Single lap offset results

Single lap offset shear tests were carried out with the scheme shown in Fig. 2a and b with or without laser surface processing, to measure the mechanical strength of similar and dissimilar joints. Fig. 8a–f shows the digital pictures of the tested samples after the mechanical tests, one for each type: Crofer/Crofer, L-Crofer/Crofer, L-Crofer/L-Crofer, Crofer/3YSZ, Crofer/L-3YSZ and L-Crofer/L-3YSZ. Observing the results of the apparent shear strength reported in Fig. 8g, one can notice that no results are shown for combinations Crofer/Crofer and Crofer/3YSZ. This is because, in those cases, no mechanical resistance was observed.

Notably, the surface tailoring using laser processing improved the mechanical resistance of the joined samples. L-Crofer/Crofer samples, presented a mechanical resistance of 27.3 ± 9.4 MPa. Fig. 8b shows that most of the sealant remained adhered to the lasered surface, indicating improved bonding and adhesion due to enhanced mechanical interlocking and demonstrating the effectiveness of laser surface processing in promoting more substantial joint integrity. The increment in apparent shear strength is even higher when both surfaces are laser processed. This is the case of the L-Crofer/L-Crofer configuration, where the mechanical resistance reached 34.8 ± 6.4 MPa. This demonstrates that laser processing enhances mechanical interlocking on both surfaces, ensuring uniform glass distribution and improved joint strength. The macrograph of the SLO sample involving two L-Crofer surfaces (Fig. 8c) showed that the glass sealant splits evenly between the two surfaces. The cohesive fracture highlights the improved bonding due to the enhanced surface roughness [21].

Similarly to what was observed for samples tested with a similar configuration, the Crofer/L-3YSZ samples presented a shear stress of 26.4 ± 6.5 MPa. The digital picture in Fig. 8e shows that in the Crofer/L-3YSZ sample, most of the glass remained attached to the lasered 3YSZ surface. This confirms the result highlighted by the test with Crofer/Crofer joined samples, where the as-received surface represents the weakest part, while the processing by laser increases strength with the glass-ceramic sealant. The L-Crofer/L-3YSZ samples (Fig. 8f) showed a mechanical resistance of 34.4 ± 4.4 MPa, similar to those obtained with an identical configuration. Moreover, the fractures are cohesive, confirming the improved strength of the interface due to the laser processing.

Fig. 9 shows the results of the FE-SEM characterisation of the fracture

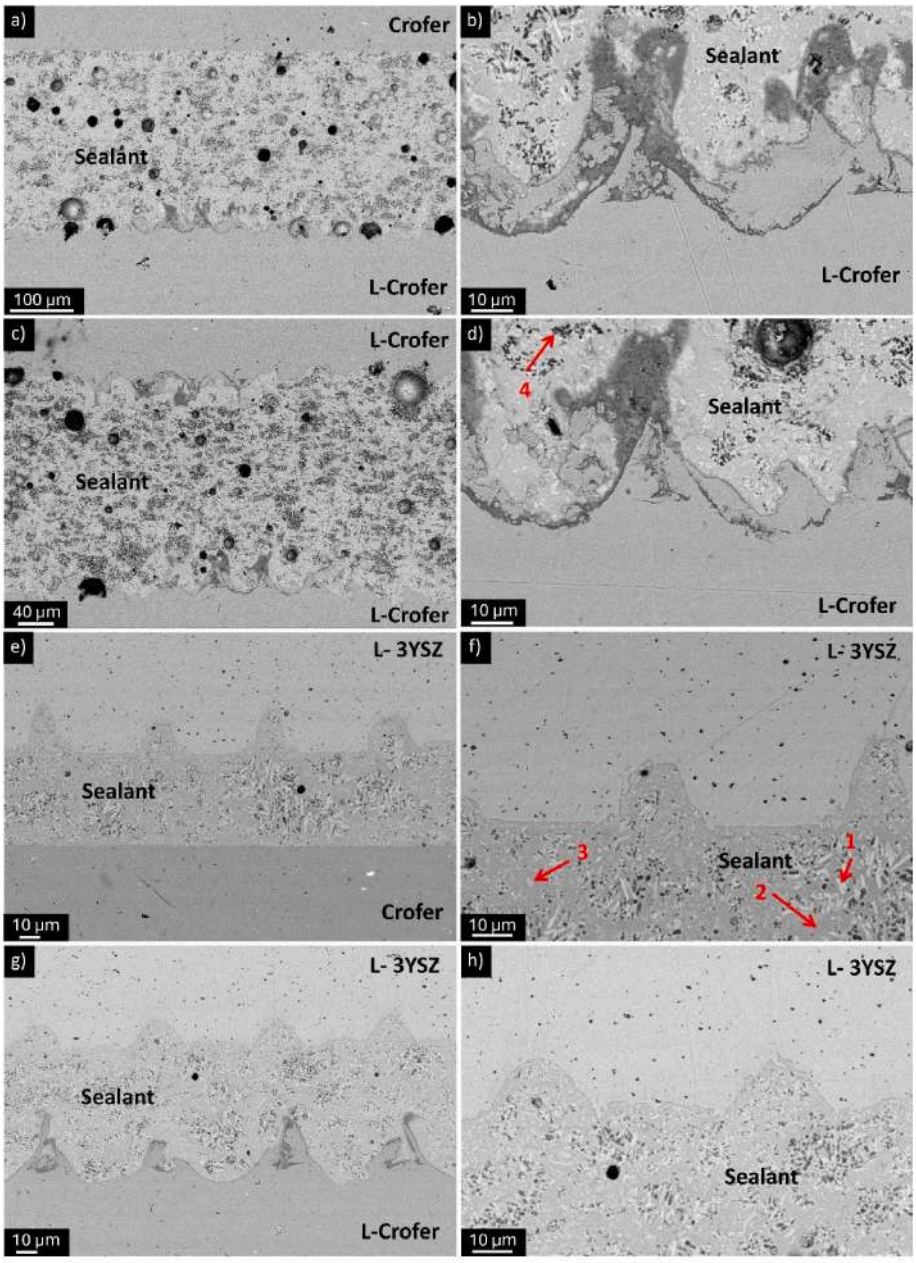

	Point 1	Point 2	Point 3	Point 4
	at%	at%	at%	at%
O	58.5	61.2	66.6	59.2
Al	1.3	1.4	0.9	1.7
Si	16.2	14.3	6.2	16.4
Ca	4.8	6.1	3.1	5.3
Zn	0.3	1.0	0.1	1.4
Y	0.2	0.2	1.2	0.1
Zr	2.5	2.5	15.5	2.1
Ba	16.2	13.3	6.4	13.8

Fig. 7. FE-SEM cross-section micrographs of (a,b) Crofer/L-Crofer, (c, d) L-Crofer/L-Crofer, (e, f) Crofer/L-3YSZ and (g, h) L-3YSZ/L-Crofer joined samples before the SLO test. EDS analyses of the glass-ceramic sealant in the joining area.

surfaces of a Crofer/L-Crofer and a L-Crofer/L-Crofer sample after the SLO test at room temperature. In the first specimen, after the test, an adhesive fracture can be observed in the cross-section's micrographs of Fig. 9a and b. All the glass remained attached to the lasered side, which presented the best adhesion due to the improved roughness. Fig. 9c and d show the cross-section of the two sides of the L-Crofer/L-Crofer sample, where the glass was equally distributed on both sides after a cohesive fracture. One can observe a regular and homogeneous layer of glass-ceramic sealant on both laser-surfaced areas. These results demonstrate that the tailoring of the surfaces makes the adhesion between the Crofer22APU and the glass-ceramic so strong that the fracture is cohesive, and the fracture occurs only through the glass-ceramic during the test. This finding means that the laser pre-treatment of the surface can effectively create a strong adhesion between the glass

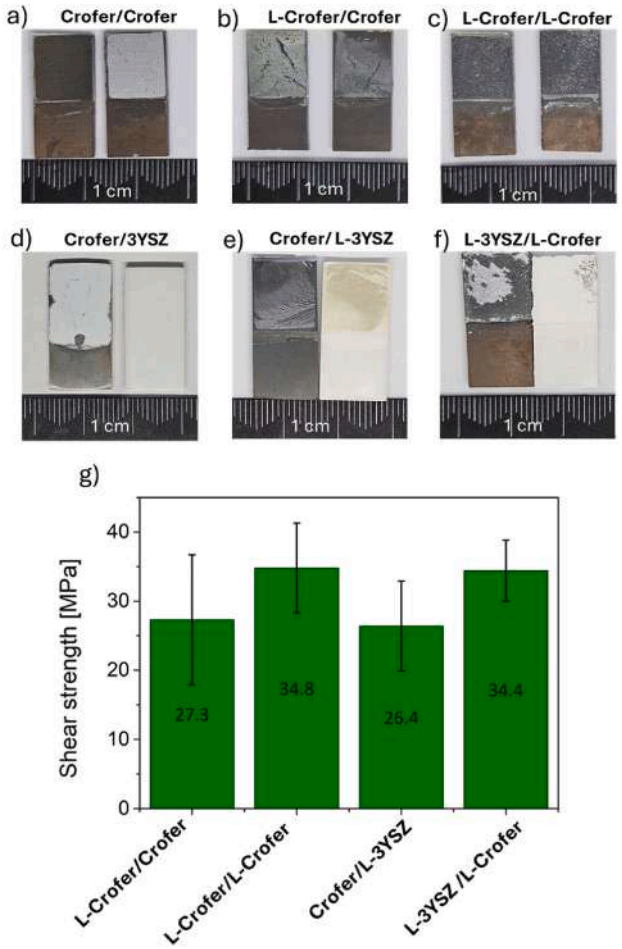

Fig. 8. Digital images of the SLO samples after the mechanical test. In the figure, the (a) Crofer/Crofer, (b) L-Crofer/Crofer, (c) L-Crofer/L-Crofer, (d) Crofer/3YSZ, (e) Crofer/L-3YSZ and (f) L-3YSZ/L-Crofer can be observed. (g) Apparent shear strength of similar and dissimilar joints produced with Crofer22APU and with 3YSZ, respectively.

sealant and the interconnect, able to withstand a considerable difference in pressure.

Fig. 10 shows the cross-section FE-SEM micrographs of the Crofer/L-3YSZ and L-3YSZ/L-Crofer samples after the mechanical test. The cross-section of the two sides after testing, i.e., Fig. 10a and b, showing Crofer and L-3YSZ, respectively, confirms the improvement of bonding when laser processing is applied. The cross-section micrographs presented in Fig. 10c and d of the L-3YSZ/L-Crofer sample show that the glass perfectly penetrated the tailored interfaces, improving the mechanical resistance, which is quite similar to the one measured for the Crofer/Crofer configuration. The glass is equally split between the two surfaces, indicating a cohesive fracture. Such a cohesive fracture in this case, as in the Crofer/Crofer configuration case, highlighted that the limit of the mechanical resistance is due to the resistance of the glass-ceramic itself and not to the interfaces.

3.6. Leakage test on Crofer22APU/3YSZ sample

Differential pressure test described in Fig. 3d was carried out at room temperature by applying different N_2 pressures and the result is shown in Fig. 11. Three measurements were carried out at 2.1 (a), 3.1 (b), and 4.1(c) bars and 15 min each for a total of 45 min. In each case, no pressure drop was detected, suggesting very high gas tightness of the tested sample and a leak rate lower than our detection limit with the current setup. This result demonstrates the robustness of the glass-ceramic sealant deposited through robocasting, a highly reproducible additive manufacturing technique. The material's ability to withstand pressure differences was significantly enhanced by employing laser patterning as a surface modification approach. These results show that these laser-patterned glass structures can endure up to 4 bars of pressure differential at room temperature without compromising their structural integrity. This achievement highlights the synergistic effect of advanced manufacturing and surface engineering for future applications integrating SOEC. The same test carried out at operating temperature is currently being studied to validate the results further at 850 °C.

4. Conclusions

Laser surface patterning was successfully applied on Crofer22APU and 3YSZ materials, achieving precise and reproducible modifications.

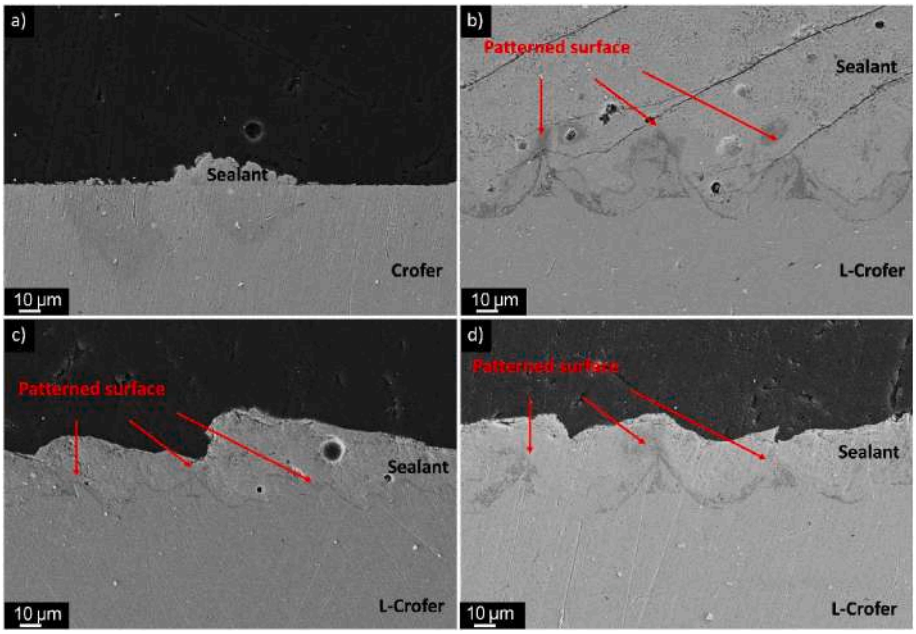

Fig. 9. FE-SEM cross-section micrographs of (a and b) a L-Crofer/Crofer sample and of (c and d) a L-Crofer/L-Crofer sample after the SLO testing.

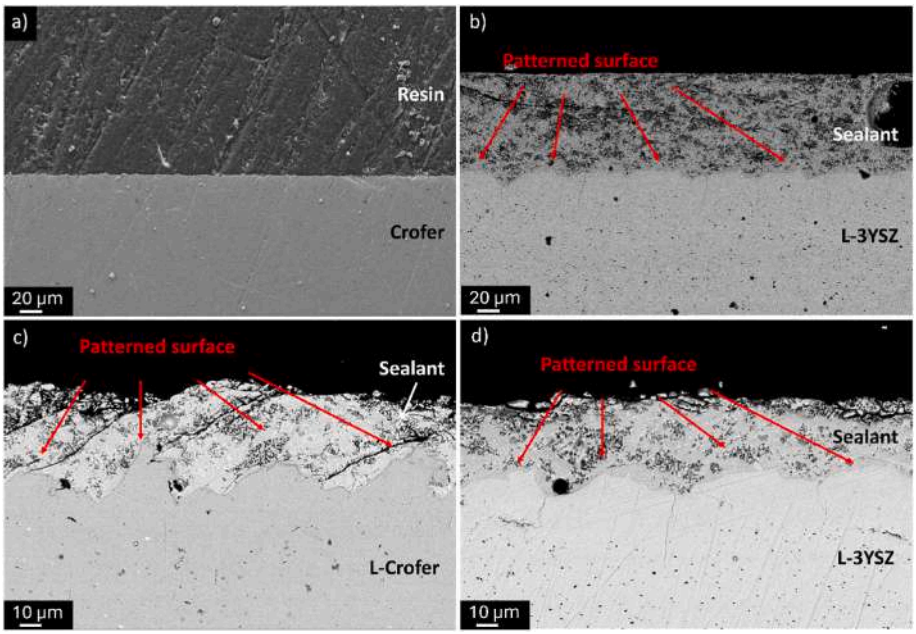

Fig. 10. FE-SEM cross-section micrographs of (a and b) a Crofer/L-3YSZ sample and of (c and d) a L-Crofer/L-3YSZ sample after the SLO testing.

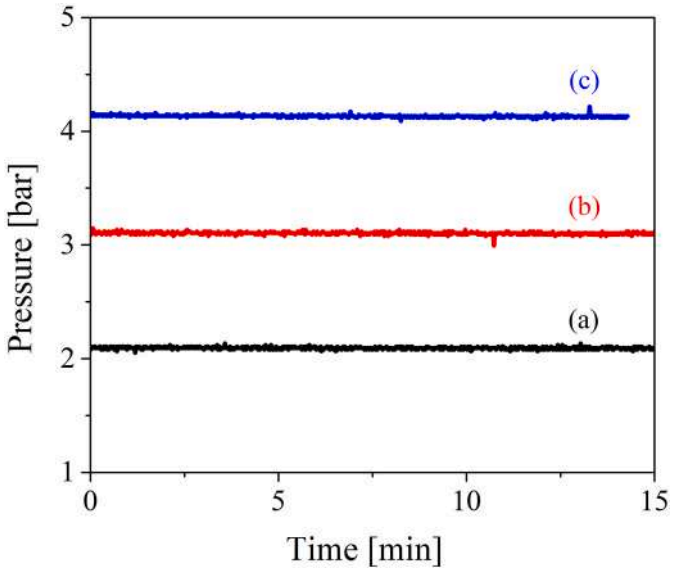

Fig. 11. Pressure drops over time measured at room temperature with N_2 at (a) 2.1, (b) 3.1 and (c) 4.1 bars on the Crofer22APU/3YSZ joined sample produced with the interlocking concept.

Mechanical testing revealed that this surface patterning technique effectively enhanced the mechanical properties of the materials, further reinforcing their structural integrity under stress. In particular, no significant mechanical resistance was measured for as-received samples, while with both Crofer/Crofer and Crofer/3YSZ, the resistance reached up to ≈34 MPa when both surfaces were lasered.

A composite glass-based paste with a 3YSZ approach, incorporating 10 wt% 3YSZ into the glass matrix. This formulation significantly increased the viscosity of the glass at high temperatures (from $10^{4.8}$ to $10^{6.1}$ Poise), enabling improved stability and performance during processing and application. The resulting paste demonstrated exceptional rheological properties (viscosity in the range 10–100 Pa s and 80 % of recovery after stress at 200 s^{-1}), making it well-suited for precision manufacturing processes such as robocasting. Notably, the laser-patterned metal and ceramic surfaces joined with the glass ceramic sealant demonstrated the ability to withstand pressure differentials of up to 4 bar, showcasing the potential of these combined approaches for developing robust and reliable components.

These findings underscore the potential of combining tailored glass-ceramic formulations with advanced surface engineering to enable reliable and durable integration of components in solid oxide electrolysis cells operating under pressure differentials.

CRediT authorship contribution statement

F. D'Isanto: Writing – review & editing, Writing – original draft, Visualization, Investigation, Formal analysis, Conceptualization. **S. Anelli:** Writing – review & editing, Writing – original draft, Visualization, Investigation, Formal analysis, Conceptualization. **F. Puleo:** Investigation. **M. Salvo:** Writing – review & editing, Supervision, Formal analysis, Conceptualization. **D.M.N. Menon:** Investigation, Formal analysis. **S. Márquez:** Formal analysis, Investigation. **D. Janner:** Conceptualization, Supervision. **E. Zanchi:** Investigation, Formal analysis. **A.G. Sabato:** Supervision, Formal analysis, Conceptualization. **A. Tarancón:** Supervision, Conceptualization. **F. Smeacetto:** Writing – review & editing, Supervision, Conceptualization.

Declaration of competing interest

The authors declare that they have no known competing financial interests or personal relationships that could have appeared to influence the work reported in this paper.

Acknowledgments

This work is part of the HyP3D (Hydrogen Production in Pressurized 3D-Printed Solid Oxide Electrolysis Stacks) project, funded by the European Union (Grant Agreement No. 101101274). Views and opinions expressed are however those of the author(s) only and do not necessarily reflect those of the European Union or Clean Hydrogen Joint Undertaking. Neither the European Union nor the granting authority can be held responsible for them. These results are also part of the Project SIMPEL, TED2021-131267B-C31, funded by MCIN/AEI/10.13039/501100011033 y por la Unión Europea "NextGenerationEU"/PRTR. A.

G. Sabato acknowledges his Ramon y Cajal fellowship RYC2021-034470-I, funded by MCIN/AEI/10.13039/501100011033 and by Unión Europea « NextGenerationEU»/PRTR». IREC also acknowledges the CERCA Programme and "Generalitat de Catalunya".

Appendix A. Supplementary data

Supplementary data to this article can be found online at https://doi.org/10.1016/j.ceramint.2025.07.326.

References

[1] Hydrogen Europe Secretariat and Revolve, Enabling a zero-emission Society, 2018.
[2] European Court of Auditors, The Eu's Industrial Policy on Renewable Hydrogen, 2024.
[3] D. Ferrero, A. Lanzini, M. Santarelli, P. Leone, A comparative assessment on hydrogen production from low- and high-temperature electrolysis, Int. J. Hydrogen Energy 38 (2013) 3523–3536, https://doi.org/10.1016/j.ijhydene.2013.01.065.
[4] Q. Li, Y. Zheng, W. Guan, L. Jin, C. Xu, W.G. Wang, Achieving high-efficiency hydrogen production using planar solid-oxide electrolysis stacks, Int. J. Hydrogen Energy 39 (2014) 10833–10842, https://doi.org/10.1016/j.ijhydene.2014.05.070.
[5] A. Pandiyan, A. Uthayakumar, R. Subrayan, S.W. Cha, S.B. Krishna Moorthy, Review of solid oxide electrolysis cells: a clean energy strategy for hydrogen generation, Nanomater. Energy 8 (2019) 2–22, https://doi.org/10.1680/jnaen.18.00009.
[6] G. Min, S. Choi, J. Hong, A review of solid oxide steam-electrolysis cell systems: thermodynamics and thermal integration, Appl. Energy 328 (2022) 120145, https://doi.org/10.1016/j.apenergy.2022.120145.
[7] J. Mermelstein, O. Posdziech, Development and demonstration of a novel reversible SOFC system for utility and micro grid energy storage, 562–570, https://doi.org/10.1002/fuce.201600185, 2017.
[8] A. Aghakhani, N. Haque, C. Saccani, M. Pellegrini, A. Guzzini, Direct carbon footprint of hydrogen generation via PEM and alkaline electrolysers using various electrical energy sources and considering cell characteristics, Int. J. Hydrogen Energy 48 (2023) 30170–30190, https://doi.org/10.1016/j.ijhydene.2023.04.083.
[9] M. El-Shafie, Hydrogen production by water electrolysis technologies: a review, Results Eng. 20 (2023) 101426, https://doi.org/10.1016/j.rineng.2023.101426.
[10] F. Smeacetto, A. Chrysanthou, A.G. Sabato, H. Javed, S.D. la Pierre, M. Salvo, M. Ferraris, Glass-to-metal seals for solid oxide cells at the Politecnico di Torino, an overview, Int. J. Appl. Ceram. Technol. 19 (2022) 1017–1028, https://doi.org/10.1111/ijac.13949.
[11] H. Javed, A.G. Sabato, I. Dlouhy, M. Halasova, E. Bernardo, M. Salvo, K. Herbrig, C. Walter, F. Smeacetto, Shear performance at room and high temperatures of glass-ceramic sealants for solid oxide electrolysis cell technology, Materials (Basel) 12 (2019), https://doi.org/10.3390/ma12020298.
[12] H. Javed, A.G. Sabato, M. Mansourkiaei, D. Ferrero, M. Santarelli, K. Herbrig, C. Walter, F. Smeacetto, Glass-ceramic sealants for SOEC: thermal characterization and electrical resistivity in dual atmosphere, Energies 13 (2020), https://doi.org/10.3390/en13143682.
[13] A. Drewniak, D. Koszelow, P. Błaszczak, K. Górnicka, K. Jurak, H. Javed, A. G. Sabato, P. Jasiński, S. Molin, F. Smeacetto, Glass-ceramic sealants and steel interconnects: accelerated interfacial stability and reactivity tests at high temperature, Mater. Des. 212 (2021), https://doi.org/10.1016/j.matdes.2021.110259.
[14] H. Javed, E. Zanchi, F. D'Isanto, C. Bert, D. Ferrero, M. Santarelli, F. Smeacetto, Novel SrO-Containing glass-ceramic sealants for solid oxide electrolysis cells (SOEC): their design and characterization under relevant conditions, Materials (Basel) 15 (2022) 1–18, https://doi.org/10.3390/ma15175805.
[15] F. D'Isanto, A. Baggio, M. Salvo, D. Basso, D. Gaia, F. Smeacetto, Glass-based sealants for joining α to β''-Al2O3 in Na–Zn batteries, Ceram. Int. 50 (2024) 14542–14549, https://doi.org/10.1016/j.ceramint.2024.01.367.
[16] R. Rechner, I. Jansen, E. Beyer, Influence on the strength and aging resistance of aluminium joints by laser pre-treatment and surface modification, Int. J. Adhesion Adhes. 30 (2010) 595–601, https://doi.org/10.1016/j.ijadhadh.2010.05.009.
[17] F. Moroni, F. Musiari, C. Favi, Influence of the laser ablation surface pre-treatment over the ageing resistance of metallic adhesively bonded joints, Int. J. Adhesion Adhes. 105 (2021) 102764, https://doi.org/10.1016/j.ijadhadh.2020.102764.
[18] L. Novák, L. Fojtl, M. Kadlečková, L. Mañas, I. Smolková, L. Musilová, A. Minařík, A. Mráček, T. Sedláček, P. Smolka, Surface modification of metallic inserts for enhancing adhesion at the metal–polymer interface, Polymers 13 (2021) 1–13, https://doi.org/10.3390/polym13224015.
[19] V. Casalegno, M. Ferraris, S. Perero, M. Suess, C. Wilhelmi, M. Pedroni, E. Vassallo, M. Salvo, A plasma pre-treatment to improve adhesion on SiC and Si3N4 ceramics, Mater. Lett. 272 (2020) 127855, https://doi.org/10.1016/j.matlet.2020.127855.
[20] I. Ritucci, R. Kiebach, B. Talic, L. Han, P. Zielke, P.V. Hendriksen, H.L. Frandsen, Improving the interface adherence at sealings in solid oxide cell stacks, J. Mater. Res. 34 (2019) 1167–1178, https://doi.org/10.1557/jmr.2018.459.
[21] F. Smeacetto, E. Zanchi, D. Meena Narayana Menon, D. Janner, S. Lamnini, M. Salvo, S. De La Pierre, H. Javed, M. Ferraris, Torsional behaviour of glass-joined, laser-processed crofer 22 APU interconnect: unravelling the effect of surface roughness on the shear strength, Ceram. Int. 48 (2022) 32837–32843, https://doi.org/10.1016/j.ceramint.2022.07.210.
[22] S. Lamnini, F. Baino, G. Montalbano, H. Javed, F. Smeacetto, Printability of carboxymethyl cellulose/glass-containing inks for robocasting deposition in reversible solid oxide cell applications, Mater. Lett. 318 (2022) 132239, https://doi.org/10.1016/j.matlet.2022.132239.
[23] S. Anelli, A. Baggio, D. Ferrero, D. Schmider, J. Dailly, M. Santarelli, F. Smeacetto, Characterization and testing of glass-ceramic sealants for protonic ceramic electrolysis cells applications, Ceram. Int. 50 (2024) 17520–17531, https://doi.org/10.1016/j.ceramint.2024.02.240.
[24] S. Anelli, M. Rosa, F. Baiutti, M. Torrell, V. Esposito, A. Tarancón, Hybrid-3D printing of symmetric solid oxide cells by inkjet printing and robocasting, Addit. Manuf. 51 (2022) 102636, https://doi.org/10.1016/j.addma.2022.102636.
[25] B.A.E. Ben-Arfa, S. Abanades, I.M.M. Salvado, J.M.F. Ferreira, R.C. Pullar, Robocasting of 3D printed and sintered ceria scaffold structures with hierarchical porosity for solar thermochemical fuel production from the splitting of CO2, Nanoscale 14 (2022) 4994–5001, https://doi.org/10.1039/d2nr00393g.
[26] M.H. Monfared, A. Nemati, F. Loghman, M. Ghasemian, A. Farzin, N. Beheshtizadeh, M. Azami, A deep insight into the preparation of ceramic bone scaffolds utilizing robocasting technique, Ceram. Int. 48 (2022) 5939–5954, https://doi.org/10.1016/j.ceramint.2021.11.268.
[27] V.G. Rocha, E. Saiz, I.S. Tirichenko, E. García-Tuñón, Direct ink writing advances in multi-material structures for a sustainable future, J. Mater. Chem. A (2020) 15646–15657, https://doi.org/10.1039/d0ta04181e.
[28] N. Kostretsova, S. Anelli, M. Nuñez, A. Morata, M. Torrell, A. Tarancón, Monolithic solid oxide cells by 3D printing, in: 15th Eur. SOFC SOE Forum, Lucerne, Switzerland, n.d.: p. A1207.
[29] S.B. Balani, S.H. Ghaffar, M. Chougan, E. Pei, E. Şahin, Processes and materials used for direct writing technologies: a review, Results Eng. 11 (2021), https://doi.org/10.1016/j.rineng.2021.100257.
[30] S. Lamnini, H. Elsayed, Y. Lakhdar, F. Baino, F. Smeacetto, E. Bernardo, Robocasting of advanced ceramics: ink optimization and protocol to predict the printing parameters - a review, Heliyon 8 (2022) e10651, https://doi.org/10.1016/j.heliyon.2022.e10651.
[31] https://www.schott.com/en-gb/products/sealing-and-solder-glass-p1000291/downloads.
[32] M.J. Pascual, A. Durán, M.O. Prado, A new method for determining fixed viscosity points of glasses, Phys. Chem. Glasses 46 (2005) 512–520.
[33] W. Conshohocken, Standard test method for strength properties of adhesive bonds in shear by, Test. 04 (1999) 6–9, https://doi.org/10.1520/D0905-08R21.1.
[34] M. Ferraris, M. Salvo, V. Casalegno, S. De La Pierre, L. Goglio, A. Benelli, Torsion test vs. other methods to obtain the shear strength of elastic-plastic adhesives, Appl. Sci. 12 (2022), https://doi.org/10.3390/app12073284.
[35] F. D'Isanto, F. Smeacetto, M.J. Reece, K. Chen, M. Salvo, Oxidation protective glass coating for magnesium silicide based thermoelectrics, Ceram. Int. 46 (2020) 24312–24317, https://doi.org/10.1016/j.ceramint.2020.06.212.
[36] F. Smeacetto, F. D'Isanto, V. Casalegno, P. Tatarko, M. Salvo, Ytterbium disilicate-based glass-ceramic as joining material for ceramic matrix composites, J. Eur. Ceram. Soc. 41 (2021) 1099–1106, https://doi.org/10.1016/j.jeurceramsoc.2020.10.022.
[37] J.E. Smay, G.M. Gratson, R.F. Shepherd, J. Cesarano, J.A. Lewis, Directed colloidal assembly of 3D periodic structures, Adv. Mater. 14 (2002) 1279–1283, https://doi.org/10.1002/1521-4095(20020916)14:18<1279::AID-ADMA1279>3.0.CO;2-A.
[38] E. Peng, D. Zhang, J. Ding, Ceramic robocasting: recent achievements, potential, and future developments, Adv. Mater. 30 (2018) 1–14, https://doi.org/10.1002/adma.201802404.
[39] M. Maillard, J. Chevalier, L. Gremillard, G.P. Baeza, E.J. Courtial, S. Marion, V. Garnier, Optimization of mechanical properties of robocast alumina parts through control of the paste rheology, J. Eur. Ceram. Soc. 43 (2023) 2805–2817, https://doi.org/10.1016/j.jeurceramsoc.2022.12.008.
[40] D. Marla, U.V. Bhandarkar, S.S. Joshi, Modeling nanosecond pulsed laser ablation: a focus on temperature dependence of material properties, Manuf. Lett. 2 (2014) 13–16, https://doi.org/10.1016/j.mfglet.2013.12.001.
[41] X. Xu, Phase explosion and its time lag in nanosecond laser ablation, Appl. Surf. Sci. 197–198 (2002) 61–66, https://doi.org/10.1016/S0169-4332(02)00304-5.
[42] C. Porneala, D.A. Willis, Observation of nanosecond laser-induced phase explosion in aluminum, Appl. Phys. Lett. 89 (2006) 1–4, https://doi.org/10.1063/1.2393158.
[43] J. Schilm, A. Rost, M. Kusnezoff, S. Megel, A. Michaelis, Glass ceramics sealants for SOFC interconnects based on a high chromium sinter alloy, Int. J. Appl. Ceram. Technol. 15 (2018) 239–254, https://doi.org/10.1111/ijac.12811.
[44] J.L. Stokes, β-Cristobalite thermal expansion and stability in environmental barrier coating systems, J. Am. Ceram. Soc. (2024) 1–8, https://doi.org/10.1111/jace.20214.